Green Chemistry

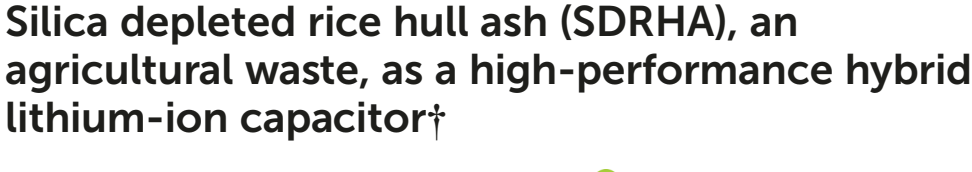


PAPER

View Article Online
View Journal | View Issue



Cite this: *Green Chem.*, 2020, **22**, 4656



Eleni Temeche, Mengjie Yu and Richard M. Laine **D**

Rice hull ash (RHA, an agricultural waste) produced during combustion of rice hulls to generate electricity consists (following dilute acid leaching) of high surface area SiO_2 (80–90 wt%) and 10–20 wt% carbon (80 m² g⁻¹ total). RHA SiO_2 is easily extracted by distillation (spirosiloxane) producing SDRHA, which offers an opportunity to develop "green" hybrid lithium-ion capacitors (LICs) electrodes. SDRHA consists of 50–65 wt% SiO_2 with the remainder carbon with a specific surface area of \approx 220 m² g⁻¹. SDRHA microstructure presents a highly irregular and disordered nanocomposite composed of nanosilica closely connected *via* graphene layers enhancing Li-ion mobility during charge/discharge process. SDRHA electrochemical properties were assessed by assembling Li/SDRHA half-cells and LiNi_{0.6}Co_{0.2}Mn_{0.2}O₂ (NMC622)-SDRHA full-cells. The half-cell delivered a high specific capacity of 250 mA h g⁻¹ at 0.5C and retained a capacity of 200 mA h g⁻¹ at 2C for 400 h. In contrast to the poor cycle performance of NMC based batteries at high C-rates, the hybrid full-cell demonstrated a high specific capacitance of 200 F g⁻¹ at 4C. In addition, both the half and full hybrid cells demonstrate excellent coulombic efficiencies (~100%). These results suggest that low cost and environmentally friendly SDRHA, may serve as a potential alternative electrode material for LICs.

Received 22nd May 2020, Accepted 26th June 2020 DOI: 10.1039/d0gc01746a rsc.li/greenchem

Introduction

Global warming provides intense motivation to find ways to supplant commercial-scale CO_2 generating processes to offset envisioned catastrophic effects on the environment. To this end, the world is rapidly adopting electric vehicles as one part of societal efforts to mitigate the anticipated rapid changes in our global environment. $^{6-10}$

The development of high rate lithium-ion batteries (LIBs) is essential to ensure the efficacy of portable electronic devices. ^{11–13} Due to their unique merits in terms of high energy density (100–250 W h kg⁻¹), wide operating voltage, and absence of memory, LIBs are now rapidly undergoing commercialization for fast charging electronics, electric vehicles, and hybrid electric vehicles. ^{14–16} However, conventional LIBs using graphite anodes cannot meet the increasing demand for power density, operational reliability, system integration, and safety requirements in many of these applications. ^{11,13,17} LIBs specific power is usually <0.5 kW kg⁻¹, with poor cycle life of <5000 cycles. ^{18,19}

Department of Materials Science and Engineering, University of Michigan, Ann Arbor. MI. 48109-2136. USA. E-mail: talsdad@umich.edu

In contrast, lithium-ion capacitors (LICs) that combine both battery and electric double-layer capacitor (EDLC) properties provide ~5-10 times greater energy densities than traditional EDLCs, higher power densities and longer cycle life than conventional LIBs. 18,20 LIC devices are desirable because they can meet the demand for high power density requirements. Typically, LICs contain a pre-lithiated anode and an EDLC cathode. 18,21-23 Extensive research has been done to optimize the electrochemical performance of hybrid-LICs. 20,24-28 Recently Zheng et al. 29 demonstrated LICs with improved specific energy through use of a hybrid positive electrode of LiNi_{0.5}Co_{0.2}Mn_{0.3}O₂ (NMC) as an additive with activated carbon. Improvements in the energy densities of LICs were achieved by optimizing the electrode components by using polymer-derived porous carbon,30 pre-lithiated graphene nanosheet,31 and "soft" carbon materials, a promising alternative to graphite for high rate applications.³²

The specific surface area (SSA) of the EDLC component is known to directly affect the electrical energy storage capacity of LICs. Hence, various porous carbon materials with the high SSAs (>1000 m² g⁻¹) have been successfully synthesized by catalytic activation,³³ carbonization of polymer blends,³⁴ and chemical vapor deposition methods.³⁵ However, these methods require complicated synthesis procedures that are high cost and/or use toxic reagents.³⁶ As a consequence, devel-

[†]Electronic supplementary information (ESI) available. See DOI: 10.1039/d0gc01746a

opment of alternative anode materials that offer high capacities, fast charge/discharge, low potentials, reduced cost of manufacturing, as well as being environmentally friendly, and safe have attracted attention from both academia and industry.^{37–39}

One less appreciated source of energy is one in which the combustion of agricultural waste is used to generate steam to produce electricity. Combustion of agricultural waste (Ag waste) such as rice hulls, corn, and coconut husks, etc. 36,40,41 takes advantage of the fact that the carbon in these sources derives directly from photosynthetic fixing of CO₂, such that the energy generated can be CO₂ neutral. Often, the combustion of Ag waste generates materials which themselves can be used to make value-added products (valorized). 40,42,43 In previous work done in this group, we demonstrated that rice hull ash (RHA), produced world-wide in millions of tons per year quantities, can be used to produce solar grade silicon (99.999% pure), 40 distillable forms of alkoxysilanes, 44 and high surface area silica for vacuum insulation panels. 45

In this work, the residual carbon recovered from distilling "silica" out of the RHA (silica depleted RHA or SDRHA) has been explored as a "green" source of anode material for high power applications. The SDRHA carbon/silica nanocomposites produced offer potential access to better, cheaper and safer EDLC electrodes while also generating value-added utility for this Ag waste. Several studies examined the advantages of RH based activated carbon as active material for the electrodes of EDLCs and LICs. 42,43,46-50 Recently, Kumagai et al. 51 demonstrated the utilization of micro and mesoporous activated carbon prepared from RH and beet sugar as the cathode material, and RH-derived C/SiOx as the composite anode material. It was revealed that the RH carbon with partially removed SiO_x (41 wt%) is a promising anode active material with high resistance to facile pre-lithiation.⁵¹ The durability against Li dendrite growth and Li-aged byproduct is attributed to the transformation of SiO_x into Li_ySiO_x , reducing the excess Li⁺-ions that could contribute to uneven Li deposition. ^{51,52} Hence, optimization of SiO_x amount in SDRHA is necessary to deliver high performance LICs.

In this study, we assess the potential of battery electrodes assembled using Li metal foil or LiNi_{0.6}Co_{0.2}Mn_{0.2}O₂ (NMC622) with SDRHA as hybrid LICs. The most significant advantage to using NMC is its high specific capacity and high voltage to enhance the energy density.29 The cell design for new generation hybrid LICs devices is discussed in detail. The specific capacity of the lithiated SDRHA is calculated to be 250 mA h g^{-1} at 0.5C and remains 200 mA h g^{-1} at 2C indicating excellent rate performance. The reversibility of Li-ion insertion in SDRHA and release of Li_vSiO_x is also discussed. The hybrid LICs assembled with NMC622 exhibit long-term cycle life, high specific capacitance of 325 F g⁻¹ at 1C, and excellent coulombic efficiency (~100%). This suggests the development of SDRHA from Ag waste is highly suitable for fabrication of supercapacitor carbon-based electrodes without prior activation.

Experimental

RHA was provided by Wadham Energy Inc. (Williams, CA). Typical impurity contents and detail analyses of RHA can be found elsewhere. 40 2-Methyl-2,4-pentanediol (hexylene glycol, ARCOS Organic) was used as received. Lithium metal foil (~750 µm), polyvinylidene fluoride ($M_{\rm w}$ ~534 kg mol⁻¹), potassium hydroxide (KOH), hydrochloric acid (HCl), and N-methylpyrrolidone (NMP) were purchased from Sigma-Aldrich (St Louis, MO). The super C65 conductive carbon black powder (\sim 62 m² g⁻¹), Celgard 2400 separator (\sim 25 μ m), and coin cell parts were purchased from MTI Corporation (Richmond, CA). The lithium nickel cobalt manganese oxide powder (NMC622) was purchased from BASF Catalysts (Cleveland, OH). The mixed solvent of ethylene carbonate (EC), dimethyl carbonate (DMC), and Ethyl methyl carbonate (EMC) (1:1:1 wt%) containing 1 M LiPF₆ as the Li salt with the addition of 10 wt% fluoroethylene carbonate was purchased from Soulbrain (Northville, MI).

Synthesis of SDRHA

SDRHA was synthesized as reported elsewhere.⁴⁸ In brief, RHA was first milled in dilute hydrochloric acid to remove impurities. RHA (200 g) was placed in a 2 L bottle with 200 g of milling media and 2 L of HCl solution (3.7 wt% HCl). Yttriastabilized zirconia, 3 mm diameter spheres was used as the media. The RHA was milled for 48 h. Thereafter, the acid milled RHA was recovered by suction filtration through a Buchner funnel. The recovered RHA was then washed with 500 mL DI water.

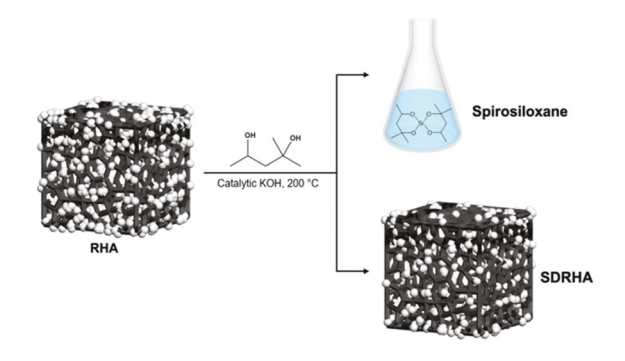
The acid milled RHA and 1 L of DI water were then introduced to a 2 L glass flask equipped with a stir bar and a reflux condenser. The suspension was then boiled for 24 h before separation by filtration through a Buchner funnel. The boiling and filter processes were repeated one more time. After the second filtration, the pH of water filtered off was neutral. Then, the RHA was dried at 100 °C in vacuum overnight.

A mixture of 250 mL hexylene glycol (HG) and 4.2 g KOH (75 mmol) was first heated to 190 °C in a 250 mL three-neck flask equipped with a stir bar to remove water for 3 h. Dried RHA powder (~50 g) was added to the HG + KOH solution. The mixture was heated to 200 °C in a pyrex distillation setup. After 100 mL HG was distilled off, another 100 mL HG was added until 500 mL HG was reacted and/or distilled out coincident with water during silica depolymerization. After 24 h, 40–50 wt% of the silica is extracted as the spirosiloxane as shown in Scheme 1. The optical images of the RHA, washed RHA, and SDRHA are presented in Fig. S1.†

Electrode preparation

In brief, SDRHA was mixed with super C65 conductive carbon and polyvinylidene fluoride (PVDF) at a weight ratio of 80:5:15 in NMP solvent, respectively. The positive electrode was prepared by mixing NMC 622 (94 wt%), super C65 conductive carbon (3 wt%), and PVDF (3 wt%) dissolved in NMP. To form uniform slurries, the two mixtures were ball-milled with

Paper Green Chemistry



Scheme 1 Synthesis of SDRHA from rice hull ash.

Al₂O₃ media (~3 mm) for 24 h, then coated onto current collectors. Copper and aluminum foils were used for the SDRHA and NMC622-based electrodes, respectively. The loading density of the active materials was in the range of 1.3-4 mg cm⁻². The electrodes were arch punched into 14 and 16 mm circle-shaped cathodes and anodes, respectively. The electrodes were then subsequently dried in a vacuum oven at 100 °C overnight prior to being transferred to an argon filled glove box.

Characterization

Fourier-transform infrared spectroscopy (FTIR). Nicolet 6700 Series FTIR spectrometer (Thermo Fisher Scientific, Inc.) was used to measure FTIR spectra. The samples (1 wt%) were mixed with KBr (International Crystal Laboratories) and were ground rigorously with an alumina mortar pestle. The chamber was purged with N2 prior to data acquisition in the range of 4000-400 cm⁻¹.

X-ray diffraction (XRD). Rigaku Miniflex diffractometer (Rigaku Denki., Ltd, Tokyo, Japan) with Cu-KR radiation (k =0.154 nm) was used to identify the phases and characterize the crystalline nature of the RHA, SDRHA, and NMC622. The diffraction data were recorded over the range of 10-70° 2θ using a scan rate of 3 min⁻¹ in 0.01 increments. The presence of crystallographic phases and their wt% fraction was refined using PDXL software (Version 2.8.4).

Specific surface area (SSA) analyses. A Micromeritics ASAP 2020 sorption analyzer was used to analyze the SSA and microporosity. Nitrogen adsorption and desorption isotherms were determined by nitrogen physisorption at -196 °C (77 K). The samples were degassed at 200 °C over 6 h prior to N2 analysis. BET method using ten data multipoint with relative pressures of 0.05-1 was used to determine SSAs.

Scanning electron microscopy (SEM). JSM-IT300HR In Touch Scope SEM (JEOL USA, Inc.) was used to analyze the microstructure of the SDRHA powders and the electrodes.

Thermogravimetric analysis (TGA). Q600 simultaneous TGA/ DSC (TA Instruments, Inc.) was used to analyze the thermal stability and determine the carbon content of SDRHA powders. Samples (15-25 mg) were hand-pressed in a 3 mm

dual-action die, and placed in alumina pans and ramped to 1000 °C at 10 °C min⁻¹ in air (60 mL min⁻¹).

X-ray photoelectron spectroscopy (XPS). Kratos Axis Ultra (Kratos Analytical) was used to determine the elements present. XPS data were collected at room temperature under 3.1×10^{-8} Pa using monochromatic Al source (14 kV and 8 mA) to record the core level element binding energies. The binding energies of all the elements were calibrated relative to the gold with Au $4f_{7/2}$ at 84 eV. All the data were analyzed by CASAXPS software.

Electrochemical measurements. The electrochemical properties of the SDRHA and NMC622 electrodes were evaluated using CR2032 coin cells. The SDRHA working electrodes were incorporated into CR2032 coin cells, in which Li metal foils (16 mm) were used as counter and reference electrodes and Celgard 2400 as separators. Before cell assembly, the metallic Li (16 mm W \times 750 μ m T) was scraped to expose a clean surface. Half-cells were constructed using a standard procedure. In addition, full cells were assembled using the SDRHA as the anode and NMC622 as the cathode. The solution of 1.1 M LiPF₆ in a mixture solvent of EC:DC:DMC (weight ratio of 1:1:1) with 10 wt% FEC additives was used as the electrolyte. The assembly process was conducted in an argon-filled glove box having O2 and H2O contents below 0.5 ppm. The coin cells were compressed at \sim 0.1 kpsi uniaxial pressure (MTI).

A SP-300 (Bio-Logic Science Instruments, Knoxville, TN) was used to measure the AC impedance, cyclic voltammetry, and galvanostatic charge/discharge. AC impedance data was recorded in a frequency range of 7 MHz to 1 Hz with an AC amplitude of 10 mV. The charge/discharge tests of SDRHA/Li and SDRHA/NMC622 were performed between 0.01-2.5 V and 2.7-4.2 V, respectively. The electrode specific capacitance was calculated according to:

$$C = \left(\int I dv\right) / (V \times m \times s) \tag{1}$$

where *I* is the current density, *V* is the potential, *s* is the potential scan rate, and m is the mass of the electroactive materials in the electrode.

Results and discussion

In the following sections, we discuss the detailed analyses of the RHA and SDRHA powders using FTIR, XRD, XPS, TGA, SEM and BET measurements. In addition, the development of a hybrid LIC system using an organic electrolyte, SDRHA as the negative electrode, Li metal, and NMC622 as the cathode is also investigated.

Characterization of RHA and SDRHA powders

Fig. 1a shows the FTIR spectra of washed RHA and SDRHA powders. The predominant band at 1090 cm⁻¹ is assigned to vSi-O-Si bonds in amorphous silica. ^{42,53} The bands located ~780 and 470 cm⁻¹ are associated with Si-O symmetric

Green Chemistry Paper

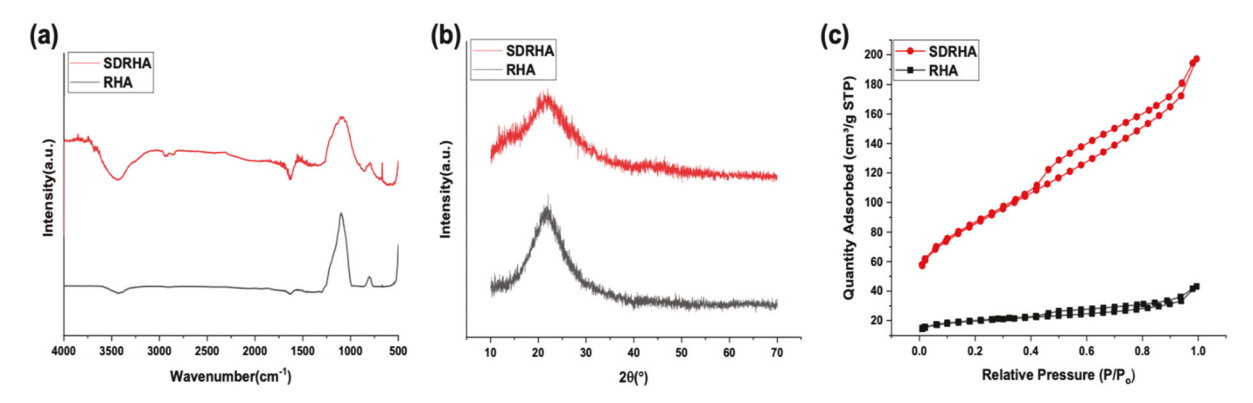


Fig. 1 (a) FTIR spectra, (b) XRD patterns, and (c) nitrogen adsorption-desorption isotherms measured on RHA and SDRHA powders.

stretching and bending vibrations, respectively. After silica removal, the remaining silica is strongly associated with residual carbon (encapsulated) and as such the degrees of freedom of the Si-O bonds are not relaxed after removal of free silica leading to a more disordered and hence broader signal. The absorption intensities of all v(Si-O-Si) vibrations are broader following silica dissolution. This is likely associated with the reduction in SiO₂ content (TGA, Fig. 2) and may also arise because of the nanoscale mixing of the remaining SiO₂ partially encapsulated in the amorphous carbon. The FTIR spectrum also indicates a small carboxyl (vC=O) peak 1550 cm⁻¹, suggesting the potential for additional pseudocapacitance, as seen previously in carbon materials.⁴³

XRD patterns of the washed RHA and SDRHA are shown in Fig. 1b. The diffraction patterns show a broad peak from ~15° to $40^{\circ} \ 2\theta$ with a central peak at $\sim 22^{\circ} \ 2\theta$ associated with amorphous phases (both carbon and SiO₂) confirming the absence of any ordered crystalline structure. 42 The weak (002) diffraction peak $\sim 22^{\circ} 2\theta$ also suggests the disordered (graphene-like) nature of the porous carbon in SDRHA. XPS studies (Fig. 3) further confirm the presence of disordered stacking of graphene layers, ascribed to the hard carbon nature of the SDRHA. These along with the hydroxyl groups at the surface suggest that SDRHA should offer superior super capacitive pro-

perties as discussed in detail in the electrochemical performance section.

Fig. 1c shows the N2 adsorption-desorption isotherms of RHA and SDRHA. The adsorption isotherms show type IV character with Type H3 hysteresis loops at a relative pressure P/P_0 between 0.4 and 1.54 Loops of this type may arise from nonrigid aggregates of plate-like particles,55 in good agreement with the morphology of the SDRHA powders as seen in the Fig. 4 SEMs. At low values of P/P_0 , the isotherms look similar to microporous adsorbents.42

The SDRHA hysteresis loop suggests the existence of mesopores, as the adsorption increases markedly above 0.4 relative pressure P/P_0 . Adsorption capacity is highly dependent on the micropore and mesopore content present in the SDRHA. The BET reported surface area of the RHA is ~80 m² g⁻¹ which is similar to that reported in the literature.⁵³ The nominal BET surface area increased from 80 to 220 m² g⁻¹ after removing SiO₂, suggesting the surface area increases with silica depletion. Hence, the amorphous silica easily dissolved during the chemical depletion process is a key factor determining the surface area of the SDRHA. The development of micropores and mesopores in SDRHA is attributed to both the intrinsic properties of hard carbon and partial removal of SiO2. The BET SSA of SDRHA (220 m² g⁻¹) is higher than what is

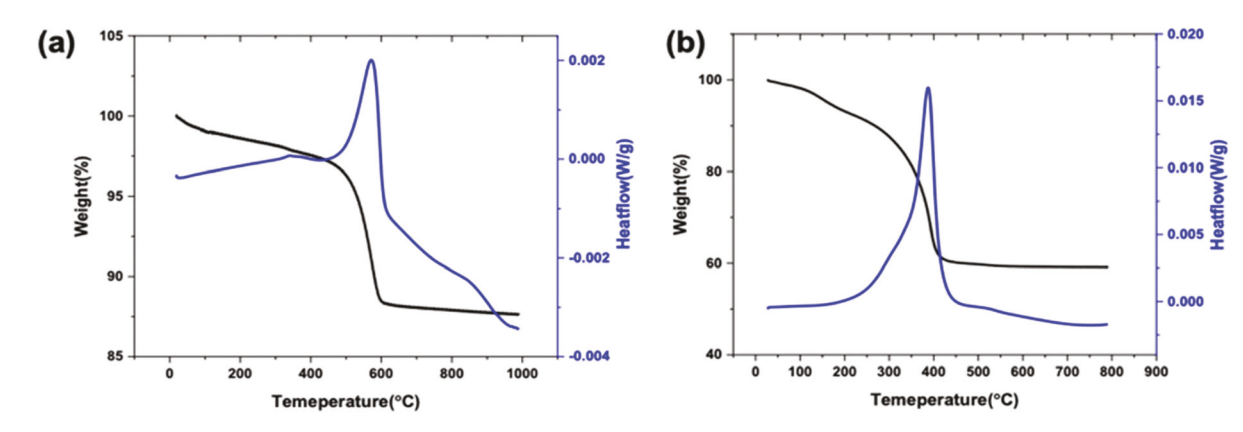


Fig. 2 TGA-DSC profile of (a) RHA and (b) SDRHA powders in air.

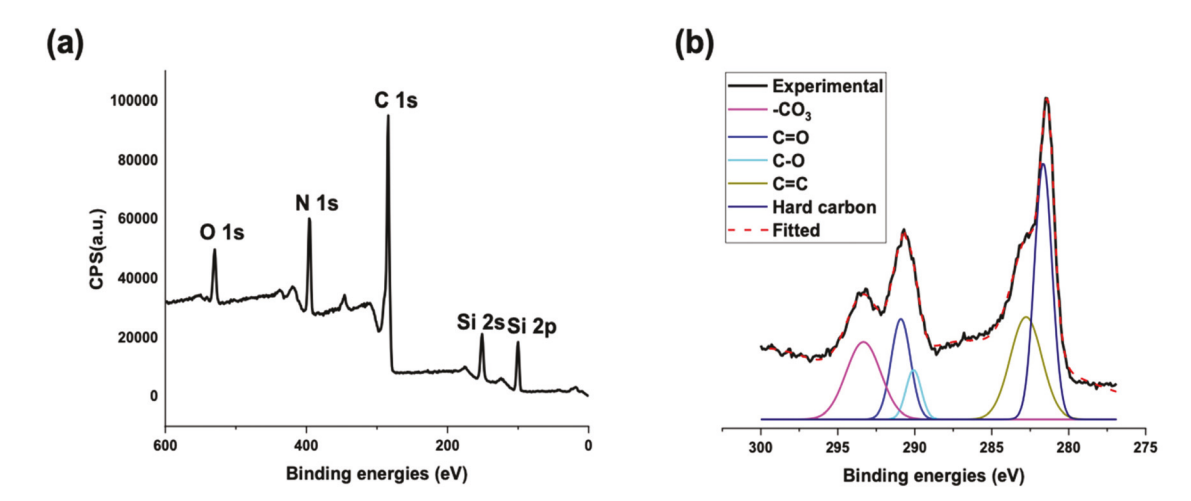


Fig. 3 (a) Wide survey XPS spectrum and (b) C 1s core-level spectrum of SDRHA powder.

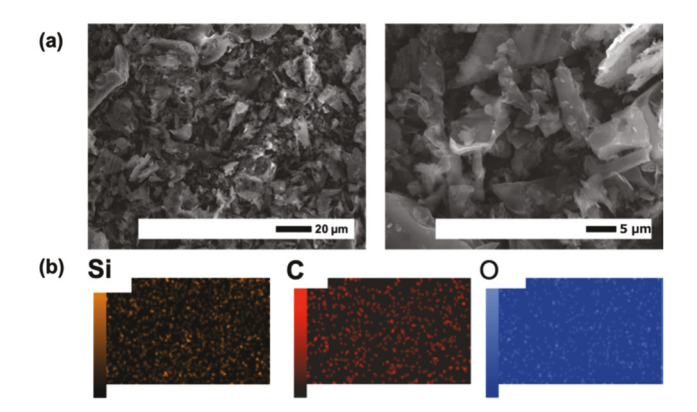


Fig. 4 (a) SEM and (b) EDX images of SDRHA powder.

reported for rice hull derived carbon (RHC, 113 m² g⁻¹), which is prepared by carbonizing RH at 600 °C per 1 h per N2 and partially leaching SiO_X by NaOH solution.⁵¹

The thermal stability of the washed RHA and SDRHA were analyzed by using TGA at 25°-800 °C in air as shown in Fig. 2. Two major mass loss regions were observed in the thermograms. The first mass loss of 2-3 wt% below 200 °C is ascribed to loss of physisorbed water and volatile compounds. The mass loss from 200°-600 °C is ascribed to oxidation of carbonaceous materials. No further obvious mass losses are observed up to 800 °C.

TGA studies were carried out to estimate the net volatile matter on the rice hull ash and the amount of carbon present in SDRHA powder. The surface carbon or the trapped carbon in the RHA is considered as an impurity. Studies show that temperature plays a significant role in the amount of carbon associated with the silica in the rice hull ash.56 The total amount of carbon in SDRHA (35-40 wt%) was calculated by subtracting the mass loss between 200°-600 °C (Fig. 2b). The final SiO2 ceramic yield was reduced from 87 to 60-65 wt% after distillative removal of silica as the spirosiloxane. The partial removal of SiO₂ is necessary to create voids to allow the volume expansion resulting from the SiO_X lithiation, which enhances the cycle life of SDRHA anode.

To further understand the surface chemistries and reaction mechanisms, XPS analysis was conducted on the SDRHA powder. Fig. 3a reveals signature, C, Si, O, and N peaks and minor Ca peaks; the latter residual from RHA.

Table S1† summarizes the XPS data. The deduced atomic composition shows 69 ± 0.3 at% carbon. It is known that photoelectrons can probe as deeply as ≈5 nm below the surface, hence a carbon 1s spectrum can provide a reasonable map of all the carbon species present.⁵⁷ Fig. 3b shows the C 1s core-level is similar that found for hard carbon electrodes.⁵⁷ The peak near 283 eV is related to hard carbon although this binding energy is lower than pristine hard carbon (284.5 eV).⁵⁷

The XPS C 1s peaks for the SDRHA can be assigned to two components-one is hard carbon and the other originates from various functional groups (i.e. C=O, C-O, and C=C) on the hard carbon surface. The literature suggests that the oxygencontaining functional groups can improve the electrochemical reactivity of hard carbon electrodes. 55

SDRHA has oxygen-containing functional groups on the carbon surface as confirmed by FTIR, XPS, and EDX in Fig. 1a, 3, and 4 respectively. The surface redox reactions can be suggested to occur between C-O functional groups and Li+ (i.e., $-C = O + Li^+ + e \leftrightarrow -C - O - Li$). The SDRHA exhibits a much larger SSA compared to washed RHA (Fig. 1c), hence one can anticipate a greater number of oxygen-containing functional groups, resulting in high specific capacity and excellent rate performance arising from surface redox reactions.

The removal of SiO2 from RHA is a simple, low cost, and eco-friendly method of producing porous functionalized hard carbon as a high-performance electrode material for hybrid LICs. In addition, as we demonstrate elsewhere, 44 the spirosiloxanes provides access to fumed silica and since it can be distilled to high purity, it also offers potential access to high purity silica in multiple forms potentially replacing

other alkoxysilanes that are currently produced from silicon metal.

Fig. 4a and b shows SEM and EDX images of SDRHA powder. SDRHA consists of particles ranging from 2 to 20 μm, with the majority in the $5-10~\mu m$ range. There is some degree of topological irregularity, the SEM microstructure shows agglomerate plate-like particles as also suggested by the BET analysis. The particle morphology was improved by ballmilling with 15 wt% PVDF binder when used to make the slurry for the hybrid LIC electrode as shown in Fig. S2.† It is known that ball-milling reduces particle irregularity and improves surface topology, resulting in an increase in packing efficiency. It is worth noting that the preparation of conventional electrodes containing carbon black is normally less elaborate.23 Fig. S2† shows the SEM fracture surface images of SDRHA electrode cast on the Cu current collector. The microstructure shows homogenous particle morphology with optimal packing efficiency. The super C65 (5 wt%) additives can be seen encompassing the SDRHA particles. This encompassing nature is highly desirable as it will establish a highly conductive route, increasing the power performance by linking more particles to form an electrically conductive network.¹⁸ The energy-dispersive X-ray (EDX) map reveals a uniform elemental distribution of Si, C, and O for the SDRHA powder.

Electrochemical performance of half-cell

Hybrid LICs refer to devices using both electrical double-layer and faradaic mechanisms to store charge. These devices are usually assembled using an electrode with an electric double layer or pseudocapacitive material combined with another rechargeable battery-type electrode. Here, the high SSA SDRHA (33 wt% C) serves as the negative electrode and Li metal or NMC622 are the battery positive electrodes. Electrochemical performance and cycling stability depend on the properties of the electrolyte used. The device capacitance relies on the nature of the contact between the electrode and electrolyte as it determines the double layer area. Organic-based electrolytes with high dielectric constants, high ionic conductivities, along with wide potential windows give rise to higher specific capacitance and energy densities compared to aqueous electrolytes. In addition, organic electrolytes fill pore areas inside the elec-

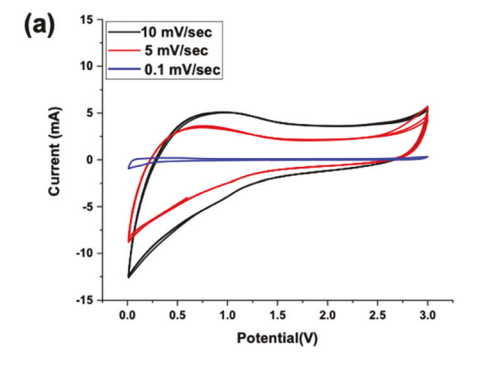
trode layers to maximize the capacitance of the active material. Hence, 1.1 M LiPF $_6$ in the mixed solvent (1:1:1 wt% ratio) EC:DEC:EMC with 10 wt% FEC was used as the electrolyte.

The CV curves, at different scan rates, elucidate the reversible surface reactions on the SDRHA porous electrode. Fig. 5a shows CV curves of SDRHA/Li cells at scan rates of 10, 5, and 0. 1 mV s⁻¹ in the potential range of 3–0.01 V. The hump at lower potential <0.5 V might be ascribed to intercalation of Li in the SDRHA layers, suggesting a faradaic mechanism. At a slower scan rate of 0.1 mV s⁻¹ (Fig. 5b), a small irreversible peak appears at 0.45 V in the first anodic process, which can be ascribed to formation of a solid electrolyte interface (SEI).⁵⁵ The CV curve from 1 to 2.7 V seems to have a rectangular shape, indicating ideal capacitive behavior.

Table 1 shows the calculated average specific capacitance of SDRHA/Li devices at various scan rates, considering the active mass of SDRHA. The high specific capacitance of ~243 F g_{SDRHA}⁻¹ is found for SDRHA/Li at 5 mV s⁻¹. For comparison, Table 2 lists typical supercapacitor systems using rice hull derived, activated carbon electrodes and their associated performance. These reported EDLCs offer high specific capacitance similar to the hybrid LICs assembled with SDRHA electrodes. Even though most of the studies demonstrate high surface area carbons from rice hulls, it was found that the specific capacitance is not linearly proportional to surface area.46 It is important to note that the specific capacitance of hybrid LICs is calculated based on the weight of SDRHA, hence it is expected to increase if one only considers the active material to be carbon (33 wt%). In addition, the electrolytes used in these systems play a great role in limiting the operating voltage of the capacitors, which limits the energy density. The cell voltage of EDLCs based on aqueous electrolyte is lower than 1 V compared to organic electrolytes (3 V).58

Table 1 Performance of SDRHA/Li cells at various scan rates

Capacitance (F g_{SDRHA}^{-1})	Scan rate (mV s^{-1})	Cell voltage	
198 ± 3	0.1	2.6	
243 ± 2	5	2.6	
182 ± 4	10	2.6	
198 ± 3 243 ± 2	5	2.6	



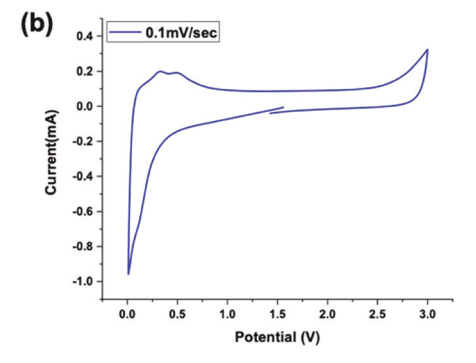


Fig. 5 (a) CV plots of SDRHA/Li half-cell in a potential range of $3-0.01\,\mathrm{V}$ at a scan rate of 10 mV s⁻¹, 5 mV s⁻¹, and (b) $0.1\,\mathrm{mV}\,\mathrm{s}^{-1}$.

Electrolyte	Electrode	Capacitance (F g ⁻¹)	Scan rate (mV s ⁻¹)	Ref.
1 M H ₂ SO ₄	Activated RHA	116 ± 2	5	65
1 M TEMABF ₄ /PC	Activated RHA	80 ± 13	5	65
6 М КОН	Nanoporous-activated RH	250	_	43
6 М КОН	Porous carbon–RH	368	2	36
3 M KCl	Activated porous carbon-RH	210	_	46
1 M Et ₄ NBF ₄ /PC	Carbon black	115	20	23
1 M LiPF ₆ EC/DMC	Graphite/activated carbon	90	5	19
0.5 M Bu ₄ NBF ₄ /ACN	PANI/graphite	420	50	66
1 M LiPF ₆ /EC/DEC	Porous carbon flakes	126	_	67
1 M TEABF ₄ /ACN	Porous carbon nanosheets	120-150	1	68
1 M TEABF ₄ /HFIP	AC	110	1	69
1 M TEABF ₄ /PC	Graphene-CNT composite	110	_	70
1.1 M LiPF ₆ /EC/DEC/EMC	SDRHA/Li	243	5	This work

 H_2SO_4 – sulfuric acid, TEMABF $_4$ – triethylmethylammonium tetrafluoroborate, PC – propylene carbonate, KOH – potassium hydroxide, KCl – potassium chloride, Et_4NBF_4 – tetraethylammonium tetrafluoroborate, DMC – dimethyl carbonate, Bu_4NBF_4 – tetrabutylammonium tetrafluoroborate, ACN – acetonitrile, HFIP – 1,1,1,3,3,3-hexafluoropropan-2-ol, and AC – activated carbon.

The electrochemical performance of the SDRHA was tested using galvanostatic charge–discharge studies at selected C-rates. Fig. 6 shows galvanostatic cycling of a SDRHA/Li half-cell between 2.5–0.01 V. The half-cell was cycled at 0.1C for 5 cycles to form a stable SEI as shown in the potential *vs.* time plot (Fig. 6b). The half-cell was then cycled at 0.5C for 20 cycles between the range of 100–150 h (Fig. 6c), 1C for 40 cycles (Fig. 6d), and 2C for 20 cycles (Fig. 6e), and finally back to 0.1C for 10 cycles.

The potential vs. time profile shows that the half-cell was cycled to the targeted potentials with minimal polarization and IR drop for 400 h. The linear symmetric potential profile at various C-rates suggests capacitance behavior in the

SDRHA/Li half-cell. The initial relatively flat plateau below 0.25 V, when cycled at a very slow scan rate of 0.1C (Fig. 6b), corresponds to reaction between Li $^+$ and the nano-SiO $_2$ in the SDRHA. In contrast, the voltage profile of the SDRHA electrode, at higher C-rates (Fig. 6c–e), slopes down during discharge without any noticeable plateau, indicating silica depletion results in a more disordered structure similar to hard carbon.

The SDRHA/Li half-cell shows an initial capacity of 1000 mA h $\rm g^{-1}$ at 0.1C (Fig. 7a), which is much larger than of the reversible capacity of hard carbon (300 mA h $\rm g^{-1}$).⁵² Hence, the extra capacity is due to the presence of nano-SiO₂ in the SDRHA powder. Recent STEM studies, done by our group,⁴⁰

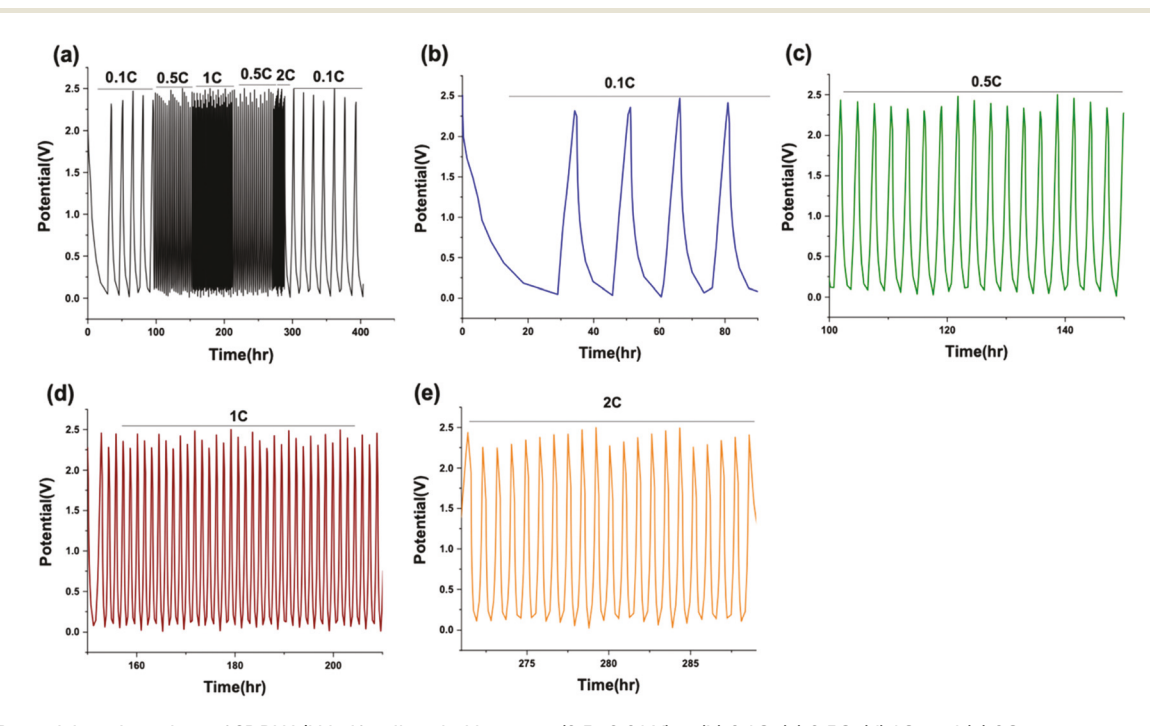


Fig. 6 (a) Potential vs. time plots of SDRHA/Li half-cell cycled between (2.5–0.01 V) at (b) 0.1C, (c) 0.5C, (d) 1C, and (e) 2C rates.

Green Chemistry Paper

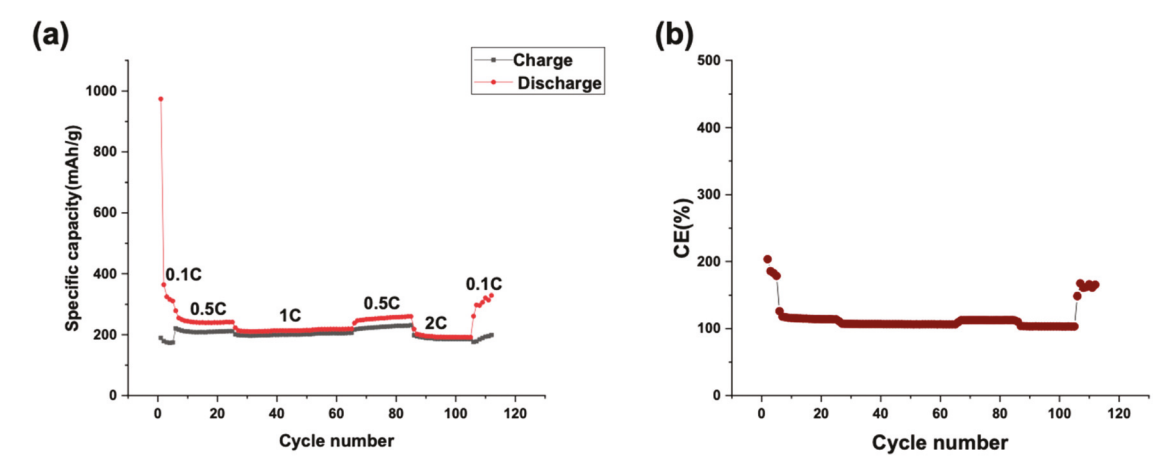


Fig. 7 (a) Galvanostatic plots of SDRHA/Li half-cell cycled between (2.5-0.01 V). The specific capacity is based on the carbon wt% in SDRHA. (b) Coulombic efficiency vs. cycle number plot.

suggest homogenous nanoscale mixing of the amorphous SiO₂ and C in RHA. The particles sizes are on the order of 20-50 nm. 40 In general, SiO₂ is believed to be electrochemically inactive for lithium storage. On the contrary, Wang et al. 52 have demonstrated that composite nano-SiO2 and hard carbon can react with Li to deliver a reversible capacity of 630 mA h g⁻¹. This means that the specific capacity of SDRHA (C_{SDRHA}) in the composite is ~1170 mA h g_{SDRHA}^{-1} which is calculated based on the reversible capacity of hard carbon $(300 \text{ mA h g}^{-1})$ and SiO_2 $(1675 \text{ mA h g}^{-1})$ as shown in eqn (2).

$$C_{\rm SDRHA} = (300~{\rm mA~h~g^{-1}} \times 0.33) + (1675~{\rm mA~h~g^{-1}} \times 0.64)$$
 (2)

The initial specific capacity of SDRHA/Li is 1000 mA h g_{SDRHA}⁻¹ which is ~85% of the theoretical capacity. However, this initial capacity is not reversible as shown by the fast capacity decay (400 mA h g_{SDRHA}⁻¹) in the second cycle, suggesting the formation of irreversible reduction of SiO2. It has been reported that amorphous nano-SiO2 can be reduced to form Si and amorphous Li₂O or crystalline Li₄SiO₄. ⁵² This irreversible formation of Li₄SiO₄ and Li₂O is supported by the CV peak and discharge plateau ~0.25 V in the initial discharge cycle as demonstrated in Fig. 5b and 6a, respectively. The reduced Si is proposed to react with Li⁺ to form Li-Si alloys resulting in the extra reversible capacity of the hybrid LICs at lower C-rate (0.1C). The formation of Li₄SiO₄/Li₂O reduces the number of excessive Li ions that could contribute to uneven Li deposition or Li-related aging byproducts.⁵¹ The initial irreversible capacity could also be attributed to the formation of SEI as supported by the current response ~0.45 V (CV, Fig. 5b). It is known that the Li ions that accumulate in the free spaces of hard carbons can be passivated. 47 Hence, the initial irreversible capacity of hard carbon is higher than graphite. 61,62 However, superior rate and cycle performance can be obtained from hard carbons, making it an attractive electrode for hybrid LICs. 63,64

The capacity decreased to 250 mA h g_{SDRHA}⁻¹ at 0.5C, the capacity further decreases to 225 mA h g_{SDRHA}⁻¹ at 1C

(Fig. 7a). The capacity loss is retained (\sim 250 mA h g_{SDRHA}^{-1}) when the C-rate was decreased to 0.5C. However, the capacity decreases to 200 mA h g_{SDRHA}⁻¹ when the C-rate was increased to 2C. Gradually, the SDRHA/Li cell shows an increase in discharge capacity (400 mA h $g_{\rm SDRHA}^{-1}$) when the C-rate is decreased back to 0.1C. The half-cell maintains a coulombic efficiency ~100% for 400 h as shown in Fig. 7b. The increase in coulombic efficiency at 0.1C is attributed to the increase in irreversible discharge capacity.

The capacity depends on the interfacial area which relies on electrode preparation such as size, shape, binder, porosity (SSA). The potential vs. time profile offers highly linear and symmetrical curves with little IR drop (0.01 V), indicating a rapid I-V response and excellent electrochemical reversibility. This is in good agreement with the obtained high coulombic efficiency.

RH-derived Si anodes have been reported to suffer from a low coulombic efficiency and limited cycle life due to high surface reactions and low thermodynamic stability.⁷¹ Embedding nano-Si in a conductive matrix is an effective way to improve the structural stability and form stable solid electrolyte interphase (SEI) films on the surface of the anode. 71

The CV (Fig. 5) and galvanostatic cycling (Fig. 7) studies demonstrate that SDRHA offers superior electrochemical properties. This enhancement in the electrode performance is attributed to the highly irregular and disordered microstructure of SDRHA, composed of closely and randomly connected graphene layers (Fig. 4), which is reported to enhance fast Liion mobility during the charge/discharge process. 60 The reversibility of Li-ion uptake and formation of Li₄SiO₄ or Li₂O could be further improved by optimizing the surface area of SiO₂ in SDRHA, which remains future work.

Electrochemical performance of full cells

The energy density of a hybrid electrochemical supercapacitor is proportional to the square of the operating voltage multiplied by the capacitance. Improving both the electrochemical

Paper Green Chemistry

stability potential window and the capacitance will greatly contribute to enhancing both energy and power densities. Hence, hybrid LICs were assembled using the high potential NMC622 cathode, and SDRHA anode with 1.1 M LiPF₆/EC/DEC/EMC electrolyte. This hybrid LIC is proposed to bridge the gap between the high energy density offered by the LIBs and the high-power densities obtained from the EDLCs. 18 The open circuit voltage increased from 2.5 to 3.2 V by exchanging the Li electrode with a high potential NMC622 cathode. Hybrid LICs have been studied extensively using composite cathode electrodes using Li-ion battery materials diluted with EDLC materials to enhance the rate performance, tap density, and increase specific capacity. 18,20,39,60 The main limitations to these hybrid LICs are the lack of composite cathode electrodes and the stability of the pre-lithiated anode.

Fig. 8a shows CV curves for SDRHA/NMC622 cells at scan rates of 5, 10, 20, 50, 100 and 500 mV s^{-1} with potential range 2.4-4.2 V. The rectangular shape of the CV curves becomes distorted with increasing scan rate. A slightly distorted and symrectangular-like shape is typical metric for electrodes. 19,53

All the CV curves do not show any redox peaks demonstrating the clear capacitance behaviour resulting from high conductivity and stable porous structure of the SDRHA electrode. Fig. 8b shows that the relationship between scan rates and peak currents are nearly linear (correlation r = 0.98), which indicates that the redox reaction is confined to the surface and not diffusion-limited.⁵⁵ Table 3 shows the calculated specific capacitance of the SDRHA/NMC622 device at various scan rates, considering the active mass of SDRHA. A high specific capacitance of ~354 F g_{SDRHA}⁻¹ is found for SDRHA/NMC622 at 5 mV s^{-1} .

The capacity ratio of the cathode to anode is calculated based on the reversible lithium intercalation and de-intercalation specific capacity of the hard carbon (\sim 300 mA h g_{carbon}^{-1}). There is a competing relationship between the ionic adsorption of the EDLC contributed by the SDRHA and the faradaic electrochemical redox reaction caused by Li-ion intercalation in the NMC622. In general, the faradaic process is suppressed by the fast surface adsorption/desorption process, thus it has

Table 3 Performance of SDRHA/NMC622 cell at various scan rates

Capacitance (F g _{SDRHA} ⁻¹)	Scan rate (mV s ⁻¹)	Cell voltage
354 ± 5	5	3.2
269 ± 2	10	3.2
184 ± 3	20	3.2
108 ± 4	50	3.2
65 ± 2	100	3.2
42 ± 6	500	3.2

been suggested that one should not fully discharge the cathode to minimize the capacity loss and maintain the high energy density.60

Hence, it is necessary to optimize the initial cycling stages. A special procedure targeting formation cycles was investigated to overcome the potential drop. The hybrid LICs were charged at 0.5C to a given voltage and allowed to relax at open circuit. Fig. S3a† shows the variation of the cell potential and its effect on formation of a stable SEI as a potential vs. time plot. The hybrid LICs voltage falls to 3.7 V during the relaxation period. It is worth noting that the total self-discharge of the hybrid LICs is the sum of the individual self-discharges taking place at each electrode. 19 Hence, the formation step (Fig. S3b†) is necessary to overcome voltage drops and minimize the self-discharge rate. The NMC/SDRHA cell showed an almost ideal linear voltage profile for the last four cycles, indicating the formation of a stable SEI. This is also supported by the increase in coulombic efficiency in the last four cycles (Fig. S3c†).

Fig. S3d† shows the specific capacity vs. cycle number. The hybrid LICs cell show an initial charge capacity of 375 mA h g⁻¹ at 0.5C. This capacity is maintained through the first 14 cycles.

The discharge capacity gradually increases from 50 to 300 mA h $\rm g^{-1}$ as the cell matures and a stable SEI forms. The specific capacitance (Fig. S3e†) also showed similar phenomena where the charge capacitance is consistent (100 F g^{-1}) and the discharge capacitance gradually increases from 25 to 100 F g⁻¹ as a stable SEI forms on the SDRHA surface. This simple formation step results in optimal behavior for the hybrid LICs as demonstrated in Fig. 9.

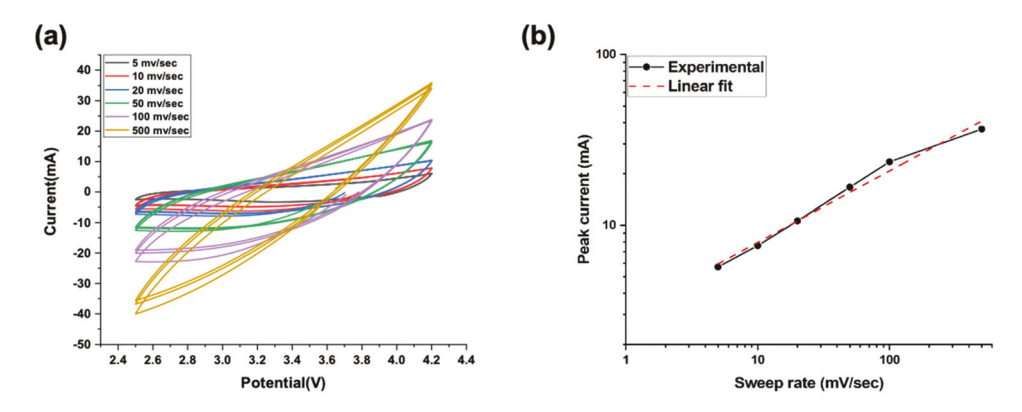


Fig. 8 (a) CV plots of SDRHA/NMC622 half-cell at different scan rates and (b) relationship between the redox peak current and scanning rates.

Green Chemistry Paper

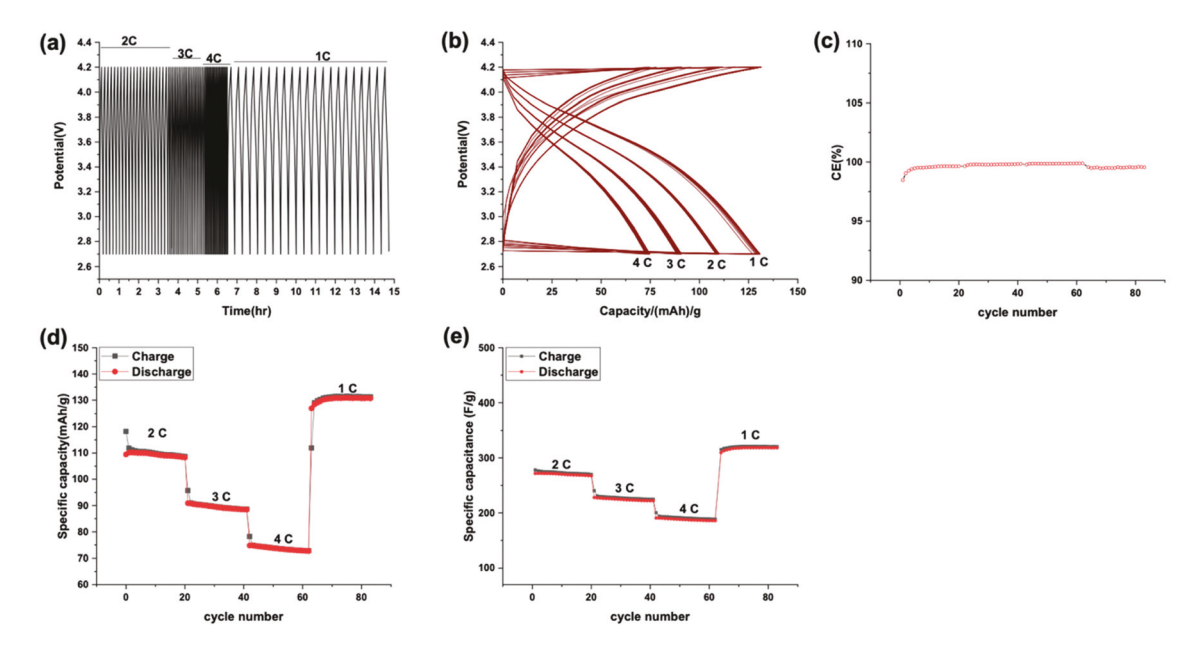


Fig. 9 Electrochemical performance of SDRHA/NMC622 cell after SEI formation. (a) Potential vs. time profile, (b) charge-discharge curves, (c) coulombic efficiency, (d) specific capacity, and (e) specific capacitance as function of cycle numbers.

Fig. 9a presents the voltage profile curves for SDRHA/NMC full-cells between 2.7-4.2 V after SEI formation. The full cell shows a linear voltage profile with a downward slope during the lithium intercalation process without showing any noticeable plateau, which is ascribed to the amorphous or disordered structure of SDRHA. The anodic/cathodic curves (Fig. 9b) of the full cell also show a linear shape indicating the capacitive nature of the device. The full cell charges and discharges to the targeted potentials without shorting at very high C-rates (1-4C).

Fig. 9d presents the galvanostatic charge-discharge cycling performance of SDRHA/NMC622 cell. The full cell was cycled at 2, 3, 4, and 1C for 20 cycles. The full cell showed an initial charge capacity of 110 mA h g⁻¹ at 2C. This capacity was maintained throughout the first 20 cycles. The capacity gradually decreased to 90 and 70 mA h g⁻¹ as the C-rate increased to 3 and 4C, respectively. The capacity increased to \sim 130 mA h g⁻¹ when the C-rate was decreased to 1C. The space gap between the adjacent carbon layers is proposed to be larger than graph-

ite, ascribed to the hard carbon nature of SDRHA, which enhances Li-ion mobility during the charge/discharge processes.

The full cell shows an initial specific capacitance of ~300 F g⁻¹ at 2C as seen in Fig. 9e. This capacity was maintained throughout the first 20 cycles. The specific capacitance gradually decreased to 250 and 200 F g⁻¹ as the C-rate increased to 3 and 4C, respectively. The capacity increased to $\sim 325 \text{ F g}^{-1}$ when the C-rate was returned to 1C. This superior rate performance is ascribed to the high surface area and microstructure of SDRHA. High efficiency of ~100% was maintained for the 80 cycles, Fig. 9c, indicating the reversibility and highpower rate performance of SDRHA/NMC hybrid LICs.

For comparison, Table 4 lists typical hybrid LICs previously reported using high potential electrodes and their associated performance. The SDRHA/NMC622 cell showed relatively higher specific capacity compared to cells assembled with activated carbons. A further improvement in energy/power density could be achieved by using composite cathodes. In the future,

Table 4 High potential-based hybrid LICs and their performance

Electrolyte	Electrode	Capacity (mA h g ⁻¹)	Ref.
1 M LiPF ₆ /EC/DMC	AC/LiFePO ₄	18	72
1 M LiPF ₆ /EC/DMC	$AC/LiNi_{0.5}Mn_{1.5}O_4$	25	21
1 M LiPF ₆ /EC/DMC/EMC	$AC + LiFePO_4/Li_4Ti_5O_{12}$	30	73
1 M LiPF ₆ /EC	$AC + LiNi_{0.5}Co_{0.2}Mn_{0.3}O_2/graphite$	80	74
LiClO ₄ /AN	AC/LiMn ₂ O ₄	106	75
1 M LiPF ₆ /EC/DMC/DEC	$AC/LiNi_{0.5}Co_{0.2}Mn_{0.3}O_2$	107	60
1 M LiPF ₆ /EC/DMC	$AC/LiNi_{0.5}Co_{0.2}Mn_{0.3}O_2$	114	76
1 M LiPF ₆ /EC/DMC	$AC/LiNi_{0.5}Co_{0.2}Mn_{0.3}O_2$	120	29
1 M LiPF ₆ /EC/DMC	$AC/LiNi_{0.5}Co_{0.2}Mn_{0.3}O_2$	225	18
1.1 M LiPF ₆ /EC/DEC/EMC	SDRHA/NMC622	130	This we

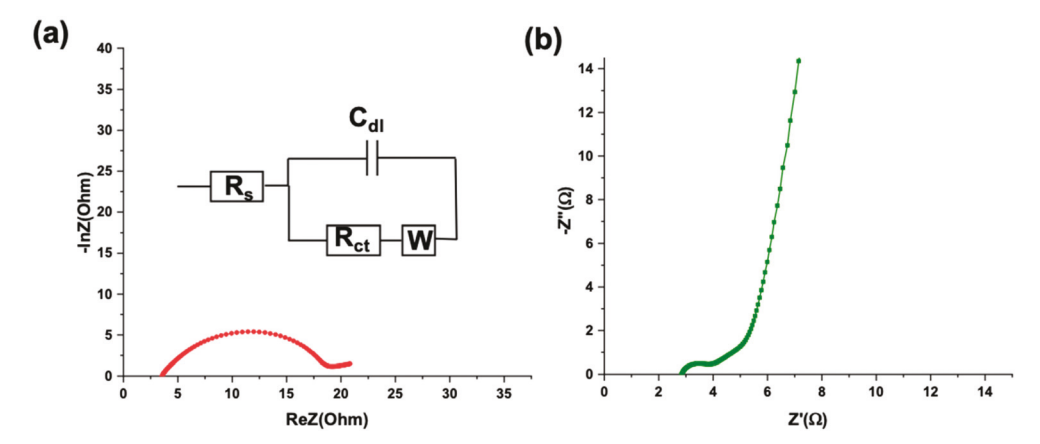


Fig. 10 Nyquist impedance spectra of (a) SDRHA/Li and (b) SDRHA/NMC. The inset shows the equivalent electrical circuit.

SDRHA/NMC composite cathodes will be investigated to enhance the double layer area and charge storage on the positive electrode.

Electrochemical impedance spectra (EIS) in the form of Nyquist plots of SDRHA/Li and SDRHA/NMC are shown in Fig. 10. In general, EIS is used to understand the electrochemical behavior at the interface between the electrode and the electrolyte. The solid electrolyte interface resistance ($R_{\rm SEI}$) is related to the high-frequency region. The lower frequency semi-circle is related to the charge transfer resistance (R_{ct}) , and the 45° capacitive slope is related to the Warburg impedance. The R_{ct} of the SDRHA with Li metal and NMC622 electrodes using organic electrolyte is presented in Table S2.† The total resistance of the half-cell is much higher than the full cell, which is ascribed to the increase in resistance between the Li metal and solid electrolyte interface, and the intrinsic resistance of the Li metal. Due to the presence of SDRHA, capacitive materials, both hybrid LICs deliver larger faradaic response than conventional batteries. The SDRHA/NMC622 cell showed an ideal capacitive behavior with a nearly vertical line parallel to the imaginary axis.

Conclusions

In summary, we have demonstrated the use of SDRHA, derived from a renewable bio-source, RHA, as a potential electrode material for hybrid LICs without any chemical activation. The high surface area and the nanostructure of the SDRHA results in high Li-ion mobility and increased surface charge absorption/desorption when assembled in both half and full-cell configurations. The cyclic voltammetry at a scanning rate of 5 mV ${
m s}^{-1}$ demonstrates a high specific capacitance of 243 and 354 F g_{SDRHA}⁻¹ for the half and full hybrid LICs, respectively. Traditional organic electrolyte based EDLCs demonstrate specific capacities in the range of 100-150 F g⁻¹. The galvanostatic charge-discharge profiles also indicate high specific capacity and excellent coulombic efficiencies. We have demonstrated the synthesis of a clean and eco-friendly electrode that is an alternative to activated carbon. Finally, SDRHA is a carbon neutral material.

Conflicts of interest

There are no conflicts to declare.

Acknowledgements

A portion of this work was also supported by a DMR NSF Grant No. DMR 099217 and Mercedes-Benz Research & Development North America, MBRDNA. We also thank the University of Michigan Energy Institute (UMEI) and Michigan Translational Research and Commercialization (MTRAC) program for support of the purchase chemicals, solvents, and furnace. We especially thank Professor Wai Lai for his insight about the SDRHA as an alternative EDLC electrode. We also like to thank Wadham Energy Inc for providing the RHA powders.

References

- 1 M. Z. Jacobson, Energy Environ. Sci., 2009, 2, 148-173.
- 2 D. B. Botkin, H. Saxe, M. B. Araújo, R. Betts, R. H. W. Bradshaw, T. Cedhagen, P. Chesson, T. P. Dawson, R. Etterson, D. P. Faith, S. Ferrier, A. Guisan, A. S. Hansen, D. W. Hilbert, C. Loehle, C. Margules, M. New, M. J. Sobel and D. R. B. Stockwell, BioScience, 2007, 57, 227-236.
- 3 G. R. Walther, E. Post, P. Convey, A. Menzel, C. Parmesan, T. J. C. Beebee, J. M. Fromentin, O. Hoegh-Guldberg and F. Bairlein, Nature, 2002, 416, 389.
- 4 J. Hansen, M. Sato, R. Ruedy, A. Lacis and V. Oinas, Proc. Natl. Acad. Sci. U. S. A., 2000, 97, 9875-9880.
- 5 T. L. Frölicher, M. Winton and J. L. Sarmiento, Nat. Clim. Change, 2014, 4, 40-44.
- 6 S. F. Tie and C. W. Tan, Renewable Sustainable Energy Rev., 2017, 76, 268-291.

Green Chemistry Paper

- 7 M. Hu, X. Pang and Z. Zhou, *J. Power Sources*, 2013, 237, 2013.
- 8 J. V. Mierlo and G. Maggetto, Fuel Cells, 2007, 7, 165-173.
- 9 N. Kamaya, K. Homma, Y. Yamakawa, M. Hirayama, R. Kanno, M. Yonemura, T. Kamiyama, Y. Kato, S. Hama, K. Kawamoto and A. Mitsui, *Nat. Mater.*, 2011, **10**, 682–686.
- 10 M. K. Hidrue, G. R. Parsons, W. Kempton and M. P. Gardner, *Resour. Energy Econ.*, 2011, 33, 686–705.
- 11 N. Nitta, F. Wu, J. T. Lee and G. Yushin, *Mater. Today*, 2015, **18**, 252–264.
- 12 L. Lu, X. Han, J. Li, J. Hua and M. Ouyang, *J. Power Sources*, 2013, 226, 272–288.
- 13 G. Zubi, R. Dufo-López, M. Carvalho and G. Pasaoglu, Renewable Sustainable Energy Rev., 2018, 89, 292–308.
- 14 Y. T. Chen, A. Jena, W. K. Pang, V. K. Peterson, H. S. Sheu, H. Chang and R. S. Liu, *J. Phys. Chem. C*, 2017, **121**, 15565– 15573.
- 15 D. A. Notter, M. Gauch, R. Widmer, P. Wäger, A. Stamp, R. Zah and H. J. Althaus, *Environ. Sci. Technol.*, 2010, 44, 6550–6556.
- 16 A. Väyrynen and J. Salminen, *J. Chem. Thermodyn.*, 2012, **46**, 80–85.
- 17 H. Buqa, D. Goers, M. Holzapfel, M. E. Spahr and P. Novák, J. Electrochem. Soc., 2005, 153, A474–A481.
- 18 M. Hagen, J. Yan, W. J. Cao, X. J. Chen, A. Shellikeri, T. Du, J. A. Read, T. R. Jow and J. P. Zheng, J. Power Sources, 2019, 433, 126689.
- 19 V. Khomenko, E. Raymundo-Piñero and F. Béguin, *J. Power Sources*, 2008, 177, 643–651.
- 20 S. R. Sivakkumar and A. G. Pandolfo, *Electrochim. Acta*, 2012, **65**, 280–287.
- 21 H. Li, L. Cheng and Y. Xia, *Electrochem. Solid-State Lett.*, 2005, **8**, 4–8.
- 22 V. Aravindan, J. Gnanaraj, Y. S. Lee and S. Madhavi, *Chem. Rev.*, 2014, **114**, 11619–11635.
- 23 A. Krause, P. Kossyrev, M. Oljaca, S. Passerini, M. Winter and A. Balducci, *J. Power Sources*, 2011, **196**, 8836–8842.
- 24 G. G. Amatucci, F. Badway, A. Du Pasquier and T. Zheng, *J. Electrochem. Soc.*, 2001, **148**, A930.
- 25 W. J. Cao, M. Greenleaf, Y. X. Li, D. Adams, M. Hagen, T. Doung and J. P. Zheng, *J. Power Sources*, 2015, **280**, 600–605.
- 26 X. Hu, Z. Deng, J. Suo and Z. Pan, *J. Power Sources*, 2009, **187**, 635–639.
- 27 P. H. Smith, T. N. Tran, T. L. Jiang and J. Chung, *J. Power Sources*, 2013, 243, 982–992.
- 28 M. Schroeder, M. Winter, S. Passerini and A. Balducci, *J. Electrochem. Soc.*, 2013, 243, 982–992.
- 29 M. Hagen, W. J. Cao, A. Shellikeri, D. Adams, X. J. Chen, W. Brandt, S. R. Yturriaga, Q. Wu, J. A. Read, T. R. Jow and J. P. Zheng, J. Power Sources, 2018, 379, 212–218.
- 30 D. Puthusseri, V. Aravindan, S. Madhavi and S. Ogale, *Electrochim. Acta*, 2014, **130**, 766–770.
- 31 J. J. Ren, L. W. Su, X. Qin, M. Yang, J. P. Wei, Z. Zhou and P. W. Shen, *J. Power Sources*, 2014, **264**, 108–113.

- 32 M. Schroeder, S. Menne, J. Ségalini, D. Saurel, M. Casas-Cabanas, S. Passerini, M. Winter and A. Balducci, *J. Power Sources*, 2014, **266**, 250–258.
- 33 M. Gozin, A. Weisman, Y. Ben-David and D. Milstein, *Nature*, 1993, **364**, 699.
- 34 N. C. Abeykoon, J. S. Bonso and J. P. Ferraris, RSC Adv., 2015, 5, 19865–19873.
- 35 K. Kobayashi, R. Kitaura, Y. Kumai, Y. Goto, S. Imagaki and H. Shinohara, *Carbon*, 2009, 47, 722–730.
- 36 H. Chen, H. Wang, L. Yang, Y. Xiao, M. Zheng, Y. Liu and H. Fu, *Int. J. Electrochem. Sci.*, 2012, 7, 4889–4897.
- 37 C. Han, H. Li, R. Shi, L. Xu, J. Li, F. Kang and B. Li, *Energy Environ. Mater.*, 2018, 1, 75–87.
- 38 A. Jagadale, X. Zhou, R. Xiong, D. P. Dubal, J. Xu and S. Yang, *Energy Storage Mater.*, 2019, **19**, 314–329.
- 39 J. Lang, X. Zhang, B. Liu, R. Wang, J. Chen and X. Yan, J. Energy Chem., 2018, 27, 43-56.
- 40 J. C. Marchal, D. J. Krug, P. McDonnell, K. Sun and R. M. Laine, *Green Chem.*, 2015, 17, 3931–3940.
- 41 R. Pode, Renewable Sustainable Energy Rev., 2016, 53, 1468–1485.
- 42 Y. Liu, Y. Guo, Y. Zhu, D. An, W. Gao, Z. Wang, Y. Ma and Z. Wang, *J. Hazard. Mater.*, 2011, **186**, 1314–1319.
- 43 H. Xu, B. Gao, H. Cao, X. Chen, L. Yu, K. Wu, L. Sun, X. Peng and J. Fu, *J. Nanomater.*, 2014, **2014**, 1–8.
- 44 R. M. Laine, J. C. Furgal, P. Doan, D. Pan, V. Popova and X. Zhang, *Angew. Chem.*, *Int. Ed.*, 2016, 55, 1065–1069.
- 45 C. D. Li, M. U. Saeed, N. Pan, Z. F. Chen and T. Z. Xu, *Mater. Des.*, 2016, **107**, 440–449.
- 46 Y. Guo, J. Qi, Y. Jiang, S. Yang, Z. Wang and H. Xu, *Mater. Chem. Phys.*, 2003, **80**, 704–709.
- 47 X. He, P. Ling, M. Yu, X. Wang, X. Zhang and M. Zheng, *Electrochim. Acta*, 2013, **105**, 635–641.
- 48 D. Liu, W. Zhang, H. Lin, Y. Li, H. Lu and Y. Wang, J. Cleaner Prod., 2016, 112, 1190–1198.
- 49 N. Isoda, R. Rodrigues, A. Silva, M. Gonçalves, D. Mandelli, F. C. A. Figueiredo and W. A. Carvalho, *Powder Technol.*, 2014, 256, 175–181.
- 50 B. Li, Z. Xiao, M. Chen, Z. Huang, X. Tie, J. Zai and X. Qian, *J. Mater. Chem. A*, 2017, 5, 24502–24507.
- 51 S. Kumagai, Y. Abe, T. Saito, T. Eguchi, M. Tomioka, M. Kabir and D. Tashima, *J. Power Sources*, 2019, 437, 226924.
- 52 B. Guo, J. Shu, Z. Wang, H. Yang, L. Shi, Y. Liu and L. Chen, *Electrochem. Commun.*, 2008, **10**, 1876–1878.
- 53 P. Prabunathan, K. Sethuraman and M. Alagar, RSC Adv., 2014, 4, 47726–47734.
- 54 K. S. W. Sing, D. H. Everett, R. A. W. Haul, L. Moscou, R. A. Pierotti, J. Rouquerol and T. Siemieniewska, *Pure Appl. Chem.*, 1985, 57, e19.
- 55 K. L. Hong, L. Qie, R. Zeng, Z. Q. Yi, W. Zhang, D. Wang, W. Yin, C. Wu, Q. J. Fan, W. X. Zhang and Y. H. Huang, *J. Mater. Chem. A*, 2014, 2, 12733–12738.
- 56 D. S. Chaudhary and M. C. Jollands, *J. Appl. Polym. Sci.*, 2004, **93**, 1–8.

- 57 H. Hori, M. Shikano, H. Kobayashi, S. Koike, H. Sakaebe, Y. Saito, K. Tatsumi, H. Yoshikawa and E. Ikenaga, *J. Power Sources*, 2013, 242, 844–847.
- 58 Y. Li, J. T. Han, C. A. Wang, H. Xie and J. B. Goodenough, *J. Mater. Chem.*, 2012, 22, 15357–15361.
- 59 A. G. Pandolfo and A. F. Hollenkamp, *J. Power Sources*, 2006, **157**, 11–27.
- 60 X. Sun, X. Zhang, H. Zhang, N. Xu, K. Wang and Y. Ma, J. Power Sources, 2014, 270, 318–325.
- 61 H. Zheng, Q. Qu, L. Zhang, G. Liu and V. S. Battaglia, *RSC Adv.*, 2012, **2**, 4904–4912.
- 62 E. Buiel and J. R. Dahn, *Electrochim. Acta*, 2004, 51, 71–80.
- 63 J. H. Kim, J. S. Kim, Y. G. Lim, J. G. Lee and Y. J. Kim, *J. Power Sources*, 2011, **196**, 10490–10495.
- 64 S. R. Sivakkumar and A. G. Pandolfo, *J. Appl. Electrochem.*, 2014, 44, 105–113.
- 65 S. Kumagai, M. Sato and D. Tashima, *Electrochim. Acta*, 2013, **114**, 617–626.
- 66 H. Zhang, J. Wang, Y. Chen, Z. Wang and S. Wang, *Electrochim. Acta*, 2013, **105**, 69–74.

- 67 J. Han, G. Xu, B. Ding, J. Pan, H. Dou and D. R. MacFarlane, J. Mater. Chem. A, 2014, 2, 5352–5357.
- 68 M. Sevilla and A. B. Fuertes, ACS Nano, 2014, 8, 5069-5078.
- 69 R. Francke, D. Cericola, R. Kötz, D. Weingarth and S. R. Waldvogel, *Electrochim. Acta*, 2012, **62**, 372–380.
- 70 N. Jung, S. Kwon, D. Lee, D. M. Yoon, Y. M. Park, A. Benayad, J. Y. Choi and J. S. Park, *Adv. Mater.*, 2013, 25, 6854–6858.
- 71 Y. Shen, J. Agric. Food Chem., 2017, 65, 995-1004.
- 72 A. Shellikeri, S. Yturriaga, J. S. Zheng, W. Cao, M. Hagen, J. A. Read, T. R. Jow and J. P. Zheng, *J. Power Sources*, 2018, 392, 285–295.
- 73 D. Ruan, Y. Huang, L. Li, J. Yuan and Z. Qiao, *J. Alloys Compd.*, 2017, **695**, 1685–1690.
- 74 X. Sun, X. Zhang, B. Huang, H. Zhang, D. Zhang and Y. Ma, J. Power Sources, 2013, 243, 361–368.
- 75 D. Cericola, P. Novák, A. Wokaun and R. Kötz, *J. Power Sources*, 2011, **196**, 10305–10313.
- 76 M. Hagen, W. J. Cao, A. Shellikeri, D. Adams, X. J. Chen, W. Brandt, S. R. Yturriaga, Q. Wu, J. A. Read, T. R. Jow and J. P. Zheng, J. Power Sources, 2018, 379, 212–218.